PAPER

Ultrahigh areal capacity and long cycling stability of sodium metal anodes boosted using a 3D-printed sodiophilic MXene/rGO microlattice aerogel†

Denghui Pan,[a] Haoyuan Yang,[a] Yueyue Liu,[a] Hui Wang, [ID][a,b] Tingting Xu,[a] Dezhi Kong,[a] Jingjing Yao, [ID][c] Yumeng Shi, [ID][d] Xinjian Li,[a] Hui Ying Yang [ID] *[c] and Ye Wang [ID] *[a,c]

Sodium metal has emerged as a highly promising anode material for sodium-based batteries, owing to its intrinsic advantages, including its high theoretical capacity, low working plateau and low cost. However, the uncontrolled formation of sodium dendrites accompanied by unrestricted volume expansion severely limits its application. To tackle these issues, we propose an approach to address these issues by adopting a three-dimensional (3D) structure of $Ti_3C_2T_x$/reduced graphene oxide ($Ti_3C_2T_x$/rGO) constructed by a direct-ink writing (DIW) 3D printing technique as the Na metal anode host electrode. The combination of the 3D-printed rGO skeleton offering artificial porous structures and the incorporation of sodiophilic $Ti_3C_2T_x$ nanosheets provides abundant nucleation sites and promotes uniform sodium metal deposition. This specially designed architecture significantly enhances the Na metal cycling stability by effectively inhibiting dendrite formation. The experimental results show that the designed $Ti_3C_2T_x$/rGO electrode can achieve a high coulombic efficiency (CE) of 99.91% after 1800 cycles (3600 h) at 2 mA cm^{-2} with 2 mA h cm^{-2}. Notably, the adopted electrodes exhibit a long life span of more than 1400 h with a high CE over 99.93% when measured with an ultra-high capacity of 50 mA h cm^{-2} at 5 mA cm^{-2}. Furthermore, a 3D-printed full cell consisting of a Na@$Ti_3C_2T_x$/rGO anode and a 3D-printed $Na_3V_2(PO_4)_3$C–rGO (NVP@C–rGO) cathode was successfully demonstrated. This 3D-printed cell could provide a notable capacity of 85.3 mA h g^{-1} at 100 mA g^{-1} after 500 cycles. The exceptional electrochemical performance achieved by the 3D-printed full cell paves the way for the development of practical sodium metal anodes.

1. Introduction

Sodium metal has received increasing attention as the anode for sodium-ion batteries (SIBs) due to its high theoretical capacity (1166 mA h g^{-1}), low redox potential (−2.71 V *vs.* the standard hydrogen electrode), and low cost.[1–5] However, the inherent high chemical reactivity of sodium and its infinite volume expansion during repeated cycling pose critical challenges such as uncontrolled growth of sodium dendrites and an unstable solid–electrolyte interphase (SEI) layer, which result in inferior cycling stability, low coulombic efficiency (CE) and even potential safety hazards.[6–14] Extensive research efforts have been devoted to addressing these issues, mainly including optimization of the electrolyte and additives, development of a stable artificial SEI, construction of three-dimensional (3D) nanostructures and design of sodiophilic interfaces.[15–24] Although numerous advancements have been achieved for sodium metal anodes, a high areal capacity with a long cycle lifespan of sodium metal anodes remains a topic requiring further exploration.

Recently, MXenes have been reported to enhance the cycling stability of sodium metal anodes by improving the sodium metal deposition behavior.[18,25,26] Among the MXene family, $Ti_3C_2T_x$ has gained significant popularity owing to its high electrical conductivity, large interlayer spacing and low Na$^+$ diffusion barrier. Furthermore, the surface of $Ti_3C_2T_x$ is functionalized with various groups (such as –F, –O) during the

[a]Key Laboratory of Materials Physics, Ministry of Education, School of Physics and Microelectronics, Zhengzhou University, Zhengzhou 450052, P. R. China. E-mail: wangye@zzu.edu.cn
[b]Center of Super-Diamond and Advanced Films (COSDAF) and Department of Chemistry, City University of Hong Kong, Hong Kong SAR, 999077, P. R. China
[c]Pillar of Engineering Product Development, Singapore University of Technology and Design, 8 Somapah Road, 487372, Singapore. E-mail: yanghuiying@sutd.edu.sg
[d]College of Electronics and Information Engineering, Shenzhen University, Shenzhen 518060, P. R. China
†Electronic supplementary information (ESI) available. See DOI: https://doi.org/10.1039/d3nr03046f

HF etching process, which makes $Ti_3C_2T_x$ sodiophilic to guide Na uniform deposition.[26–30] Owing to these advantages, $Ti_3C_2T_x$ has been investigated as a stable host for sodium metal anodes.[31,32] For example, Fang *et al.* emphasized the role of –F and –O functional groups in promoting Na deposition by evaluating the adsorption energies of F–Na and O–Na.[27] He *et al.* proved that sodium deposition can be improved by introducing hydroxylated $Ti_3C_2T_x$ with a higher concentration of –O functional groups.[33,34] Thus, h-Ti_3C_2/CNT/Na anodes can stably operate for more than 4000 h at 1.0 mA cm^{-2} with 1.0 mA h cm^{-2}.[35] By structure optimization, stepped sodiophilic gradient structure-based Na metal anodes even can cycle for 180 h at a high current density of 40 mA cm^{-2} with 40 mA h cm^{-2}.[36] Moreover, surface functionalization of $Ti_3C_2T_x$ incorporated with other nanostructures leads to more uniform deposition of Na, such as Mg^{2+}-decorated Ti_3C_2 MXenes,[37] $Ti_3C_2T_x$-modified carbon cloth,[38] $Ti_3C_2T_x$-derived 1D/2D hybrid nanostructures,[39] and 3D Ti_3C_2MXene@g-C_3N_4 heterogeneous nanostructures.[33] Although these pioneering studies explored the possibility of using $Ti_3C_2T_x$ for Na metal anodes and investigated the related mechanism, achieving a high areal capacity with a long life span for sodium metal anodes remains a challenge.[38]

Herein, a 3D $Ti_3C_2T_x$/reduced graphene oxide ($Ti_3C_2T_x$/rGO) microlattice aerogel was constructed by a direct-ink writing (DIW) 3D printing technique and further adopted as the sodiophilic skeleton for the Na metal anode. 3D printing technology is a new free-form manufacturing technology that creates artificial complex architectures, such as a microlattice structure. A 3D-printed microlattice structure has a periodic hierarchical structure with good mechanical strength, which is suitable as the host of sodium metal anodes.[40] Moreover, a 3D-printed microlattice provides a large areal capacity by increasing the printed layers and a high rate capability by using conductive and sodiophilic materials.[18,41] This specially dedicated $Ti_3C_2T_x$/rGO microlattice aerogel features a periodic hierarchical structure with sub-millimeter microchannels and micrometer pores, providing a large specific surface area that can effectively reduce the local current density to enlarge the dendrite nucleation Sand's time.[42–46] The periodical porous structure of the 3D-printed aerogel not only promotes the contact between the electrode and electrolyte, but also accommodates the large volume expansion.[41,47–50] Furthermore, the abundant functional groups on $Ti_3C_2T_x$ provide plenty of active nucleation sites, leading to uniform sodium deposition to inhibit dendrite formation. Benefiting from these advantages, the prepared 3D-printed $Ti_3C_2T_x$/rGO microlattice aerogel exhibited excellent electrochemical performance. For instance, it can stably operate for 1800 cycles at 2 mA cm^{-2} with 2 mA h cm^{-2} with a high average CE of 99.91%. Moreover, the 3D-printed $Ti_3C_2T_x$/rGO aerogel even can stably operate for 1400 h at an ultrahigh areal capacity of 50 mA h cm^{-2} at 5 mA cm^{-2}. Furthermore, a 3D-printed full cell configuration consisting of a Na@$Ti_3C_2T_x$/rGO anode and a $Na_3V_2(PO_4)_3$@C/rGO (NVP@C/rGO) cathode was used to demonstrate the practicality. The full cell can deliver a capacity of 85.3 mA h g^{-1} at 100 mA g^{-1} with a capacity retention of 91.6% after 500 cycles. Our results prove that the 3D-printed $Ti_3C_2T_x$/rGO microlattice aerogel is promising for high performance Na metal anodes.

2. Experimental

2.1 Synthesis of $Ti_3C_2T_x$ nanosheets

The synthesis process of $Ti_3C_2T_x$ Nanosheets can be found in the previous reports.[51] In brief, 2 g of LiF was dissolved in 30 mL of 9 M HCl solution and stirred for 20 min. Then 1 g of Ti_3AlC_2 (purchased from Jilin 11 Technology Co., Ltd) powder was added to the above solution and stirred vigorously at 40 °C for 24 h. After that, the solution was spun at 3500 rpm for 10 min, followed by rinsing with deionized (DI) water and centrifuged at 3500 rpm until pH ∼ 6. The precipitate was collected and then re-dispersed in DI water, passed through nitrogen in an ice bath and sonicated for 30 min. The resulting suspension was centrifuged at 3500 rpm for 1 h. The supernatant was re-dispersed in DI water with a concentration of 1 mg mL^{-1}.

2.2 Preparation of the $Ti_3C_2T_x$/GO ink and 3D-printed $Ti_3C_2T_x$/GO microlattice aerogel

GO with a concentration of 10 mg mL^{-1} was prepared by a modified Hummers' method.[52] $Ti_3C_2T_x$/GO ink was prepared by adding $Ti_3C_2T_x$ solution to the GO solution with various $Ti_3C_2T_x$ mass ratios (30%, 50%, 70%) to the whole mass under vigorous stirring for 30 min. The mixture was then subjected to high-speed centrifugation to remove excess water, and the resulting $Ti_3C_2T_x$/GO ink was collected for further processing. The DIW 3D printing process was carried out using a multi-axis dispensing system (MUSASHI, SM200SX-3A). The 3D printing parameters can be found in our previous reports.[18,41,53] The printing speed was set as 10 mm s^{-1}. After the printing process, the microgrid hydrogel were freeze-dried in a freeze dryer at −40 °C for 48 h to remove the water. Finally, the freeze-dried samples were annealed in a tube furnace at 450 °C for 2 h with a ramping rate of 1 °C s^{-1} in an Ar gas environment to reduce $Ti_3C_2T_x$/GO to a $Ti_3C_2T_x$/rGO microlattice for the final desired electrodes.

2.3 Material characterization

The morphology of the electrodes was analyzed by scanning electron microscopy (SEM, JEOL, JSM-6700F), transmission electron microscopy (TEM, JEOL, JEM-2100) and high-resolution TEM (HRTEM). Energy dispersive X-ray spectroscopy (EDS) was performed by using an EDX module integrated on SEM equipment. The crystal structures of rGO and $Ti_3C_2T_x$/rGO samples were examined using XRD (SmartLab 3 kW) operated at 40 kV using Cu Kα radiation. Thermogravimetric analysis (TGA) was conducted using a Discovery SDT650 (TA Instruments) from room temperature to 800 °C in air with a ramping rate of 10 °C min^{-1}. X-ray photoelectron spectroscopy (XPS) qualitative analysis was carried out on a Thermo FEI 250Xi device. Surface area measurements were carried out

through N_2 physical adsorption at 77 K using the Brunauer–Emmett–Teller (BET, ASAP 2420, Micromeritics) method.

2.4 *In situ* optical microscopy measurements

The morphology evolution of the electrodes was investigated by *in situ* optical microscopy measurement using a visualization unit attached to an optical microscope (Cewei, LW750LJT). The observation cell comprises a working electrode (Cu, rGO or $Ti_3C_2T_x$/rGO), a counter electrode (a piece of sodium foil) and a physical separator. The cell was filled with 300 μL electrolyte (1 M $NaPF_6$ in diglyme) and sealed with a piece of sapphire. The entire process was conducted in a glove box.

2.5 Fabrication of Na@$Ti_3C_2T_x$/rGO anodes and electrochemical performance evaluation

Na metal was deposited into $Ti_3C_2T_x$/rGO to form Na@$Ti_3C_2T_x$/rGO anodes through an electrochemical deposition process with $Ti_3C_2T_x$/rGO, Na foil and a piece of Celgard 2500 as the working electrode, counter electrode and separator, respectively. 1 M $NaPF_6$ in diglyme was used as the electrolyte. The electrodeposition process was conducted *via* a battery discharge/charge equipment (Neware, Shenzhen). Before electrodeposition, the cells underwent a pretreatment step with a current density of 100 μA cm^{-2} for 5 cycles in the voltage range of 0–1 V (*vs.* Na$^+$/Na) to form stable solid–electrolyte interface (SEI) films on the surface. Long cycling stability measurements were performed at 2 mA cm^{-2} with 2 mA h cm^{-2}, 5 mA cm^{-2} with 20 mA h cm^{-2}, and 5 mA cm^{-2} with 50 mA h cm^{-2}. The long cycle performance was also measured at 2 mA cm^{-2} with 2 mA h cm^{-2} based on the symmetrical cells by pre-deposition of 8 mA h cm^{-2} Na into the $Ti_3C_2T_x$/rGO electrode by the electrochemical deposition method. Electrochemical impedance spectroscopy (EIS) was carried out in the frequency range of 100k–0.01 Hz using an electrochemical workstation (VMP3, Bio-logic).

2.6 Assembly of the full cell and electrochemical performance evaluation

The preparation process of the 3D-printed NVP@C–rGO cathode can be found in our previous studies.[18] A full cell assembled with NVP@C–rGO as the cathode and Na@$Ti_3C_2T_x$/rGO as the anode, which was prepared by depositing 2 mA h cm^{-2} Na onto the $Ti_3C_2T_x$/rGO electrode at a current density of 0.1 mA cm^{-2} for 20 h with a deposition capacity of 2 mA h cm^{-2}. The full cell set was mounted in a CR2032 coin cell in a glove box, and its performance was evaluated in the voltage range of 3.8–2.0 V. The capacity of the cell was calculated based on the mass of NVP@C.

3. Results and discussion

The preparation process of the 3D-printed $Ti_3C_2T_x$/rGO microlattice aerogel is illustrated in Fig. 1a. First, few-layer $Ti_3C_2T_x$ nanosheets were prepared by etching away the Al in Ti_3AlC_2 using a LiF and HCl mixture, resulting in $Ti_3C_2T_x$ nanosheets rich in functional groups such as –O, –OH, and –F.[34] Fig. S1†

shows a typical few-layer $Ti_3C_2T_x$ nanosheet with a lattice spacing of 1.05 nm. Owing to these hydrophilic functional groups, the MXene aqueous solution can be naturally prepared without additives.[54] Next, the printable inks can be simply prepared by mixing GO and $Ti_3C_2T_x$ nanosheets with various ratios, followed by the removal of excess water through high-speed centrifugation. Then, a $Ti_3C_2T_x$/GO hydrogel was printed using a DIW 3D printer with the prepared inks. The hydrogel was freeze-dried to eliminate the water to prepare the $Ti_3C_2T_x$/GO aerogel. Finally, the prepared $Ti_3C_2T_x$/GO aerogel was reduced into the $Ti_3C_2T_x$/rGO aerogel by annealing at 450 °C in Ar/H$_2$ (95/5%) gas. It is worth mentioning that 3D printing technology can easily fabricate artificial $Ti_3C_2T_x$/rGO electrodes with various patterns, sizes and thicknesses as shown in Fig. S2.† In this experiment, $Ti_3C_2T_x$/rGO microlattice aerogels with a size of 1 × 1 cm and a thickness of 1.5 mm were used for further characterization and performance evaluation. In addition, the 3D-printed $Ti_3C_2T_x$/rGO microlattice aerogels show ultra-light weight properties, which can be demonstrated by being supported on a dandelion (Fig. S3†).

The morphology of 3D-printed 50% $Ti_3C_2T_x$/rGO microlattice aerogels is shown in Fig. 1b–d. The 3D-printed 50% $Ti_3C_2T_x$/rGO microlattice aerogel is composed of periodic sub-millimeter microchannels and approximately 350 μm filaments with corrugated graphene nanoflakes and abundant micropores. The periodic microchannels and micropores can accelerate the transportation of the electrolyte carried with Na$^+$ ions, and provide plenty of cavities for Na metal accommodation during repeated cycling.[19] $Ti_3C_2T_x$ nanosheets with an average size of 50 nm are uniformly distributed on the surface of rGO, which is shown in the TEM image (Fig. 1e). The crystal lattice spacings of 0.26 and 0.34 nm correspond to the (010) crystal plane of $Ti_3C_2T_x$ and the (002) crystal plane of rGO (Fig. 1f).[40,55] In addition, the Ti, C, F and O elements are uniformly distributed in the 3D-printed $Ti_3C_2T_x$/rGO microlattice aerogels as shown in the EDS elemental mapping in Fig. 1g. The 3D-printed rGO, 30%, and 70% $Ti_3C_2T_x$/rGO aerogels exhibit a similar morphology to that of the 50% $Ti_3C_2T_x$/rGO aerogel as shown in Fig. S4–S6.†

Fig. 2a shows the XRD patterns of 3D-printed $Ti_3C_2T_x$/rGO microlattice aerogels. A sharp peak centered at 25.32° is observed in rGO nanocomposites, which can be attributed to the (002) crystal planes of rGO.[40] A large peak located at 9.0° is found in the $Ti_3C_2T_x$ nanocomposites corresponding to the (002) crystal plane of $Ti_3C_2T_x$, indicating the successful synthesis of the few-layer $Ti_3C_2T_x$ MXene.[27] It is also found that the peak intensity of $Ti_3C_2T_x$ increased with the increase of $Ti_3C_2T_x$ ratio. TGA was used to measure the ratio in the hybrid nanocomposites as shown in Fig. 2b. From the TGA curves, the weight loss before 100 °C and from 100 to 520 °C can be attributed to the evaporation of moisture and the oxidation of rGO.[6] Therefore, the $Ti_3C_2T_x$ ratios in the 30%, 50% and 70% $Ti_3C_2T_x$/rGO nanocomposites are 32.5%, 48.3%, 71.6%, respectively, which is agreed well with the initial ratios. The specific surface areas of the 3D-printed rGO, 30%, 50% and 70% $Ti_3C_2T_x$/rGO, are 281.47, 242.59, 175.72 and 138.39 m^2
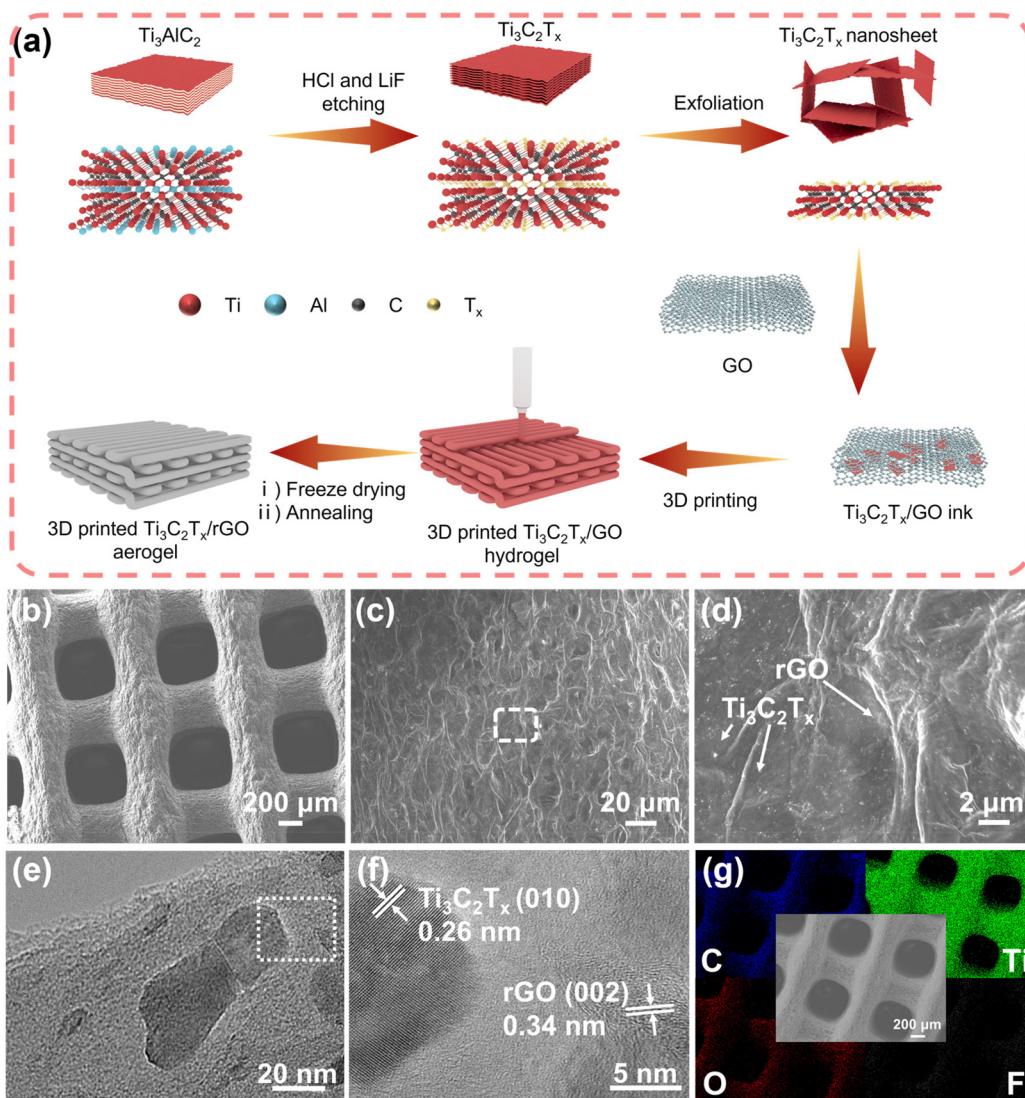
Fig. 1 (a) A schematic diagram of the preparation process of 3D-printed $Ti_3C_2T_x$/rGO microlattice aerogel electrodes. (b–d) SEM and (e and f) TEM images of the 3D-printed 50% $Ti_3C_2T_x$/rGO electrode. (g) SEM image of the 3D-printed 50% $Ti_3C_2T_x$/rGO microlattice aerogel and the corresponding EDS elemental mapping.

g^{-1}, respectively (Fig. 2c). It is worth mentioning that the 3D-printed 50% $Ti_3C_2T_x$/rGO aerogel exhibits the highest average pore size of 10.56 nm among the prepared 3D-printed electrodes (Fig. S7†). The $Ti_3C_2T_x$ MXene surface functional groups were characterized by XPS, as shown in Fig. 2d–f and Fig. S8.† There are four peaks in C 1s XPS spectrum, which are C–Ti (282.1 eV), C–C (284.7 eV), C–O (286.0 eV) and C=O (288.3 eV) (Fig. 2e).[56] In the Ti 2p spectrum, there are four pairs peaks belonging to Ti–C (455.2 and 461.3 eV), Ti^{2+} (455.7 and 461.9 eV), Ti^{3+} (456.9 and 463.2 eV) and TiO_2 (459.5 and 464.8 eV) (Fig. 2f). F 1s has two peaks at 685.1 and 686.2 eV corresponding to the F–Ti bond and the F–Al bond, respectively (Fig. S8†).[27,38,56]

The electrochemical performance of the prepared electrodes was evaluated based on a half-cell configuration as depicted in Fig. 3. Rate performance measurement was per-formed at a plating/stripping capacity of 2 mA h cm^{-2} at various current densities from 0.5 to 5 mA cm^{-2} (Fig. 3a). The 2D planar copper foil electrodes exhibited the worst perform-ance with high overpotentials of 38.7 and 40.6 mV at 0.5 and 1 mA cm^{-2}, respectively (Fig. S9a†), and it is even short-circuited when the current density increased to 2 mA cm^{-2}. In contrast, the 3D-printed electrodes demonstrated improved electrochemical performance compared to the copper foil elec-trodes. For example, the nucleation overpotentials of 3D-printed rGO are 16.4, 23.6, 30.3, 43.4 and 51.6 mV at 0.5, 1, 2, 4, and 5 mA cm^{-2} (Fig. S9b†). The 3D-printed 50% $Ti_3C_2T_x$/rGO electrode exhibits nucleation overpotentials of 6.5, 9.3, 11.5, 16.0, and 21.4 mV at the same measurement current den-sities, respectively (Fig. 3b). The nucleation overpotentials of the 3D-printed 30% and 70% $Ti_3C_2T_x$/rGO electrodes are shown in Fig. S9c and d.† The nucleation overpotentials of
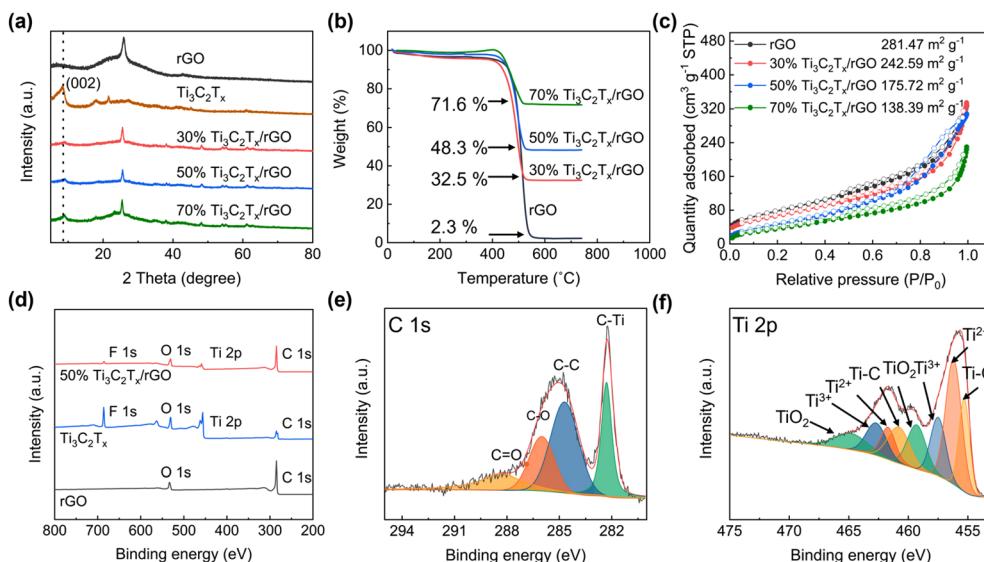
**Fig. 2** (a) XRD patterns of rGO, $Ti_3C_2T_x$ and $Ti_3C_2T_x$/rGO nanocomposites. (b) TGA curves of rGO and $Ti_3C_2T_x$/rGO nanocomposites. (c) N_2 adsorption/desorption isotherms of rGO and $Ti_3C_2T_x$/rGO nanocomposites. (d) XPS survey spectra of rGO, $Ti_3C_2T_x$ and $Ti_3C_2T_x$/rGO nanocomposites. (e) C 1s and (f) Ti 2p XPS spectra of $Ti_3C_2T_x$ nanocomposites.

various electrodes at various current densities are compared as shown in Fig. 3c, it is clear to see that the 50% $Ti_3C_2T_x$/rGO electrode shows the smallest nucleation overpotentials at all measured current densities. The nucleation overpotentials are reduced with the increase of $Ti_3C_2T_x$ owing to the sodiophilicity property of $Ti_3C_2T_x$ when compared with those of rGO and 30% $Ti_3C_2T_x$/rGO aerogel electrodes.[38] The nucleation overpotential of the 3D-printed 50% $Ti_3C_2T_x$/rGO electrode is lower than that of the 70% $Ti_3C_2T_x$/rGO electrode which may be due to that the 3D-printed 50% $Ti_3C_2T_x$/rGO electrode has a larger specific surface area.[19] The porous microlattice aerogel structure of 50% $Ti_3C_2T_x$/rGO can effectively improve ion flow transport and sodium ion distribution, which directly leads to the lowest nucleation overpotentials at all current densities.[41]

To evaluate the reversibility of the electrode, CE was determined through constant current charge–discharge (GCD) measurements as shown in Fig. 3d, e and Fig. S10, S11.† When operated at 2 mA cm^{-2} with 2 mA h cm^{-2}, the CE of the 2D planar copper foil was extremely unstable during cycling, reaching as low as 49.27% and short-circuited after only 190 cycles (Fig. 3d). The main reason for the low and unstable CE is the formation of sodium dendrites caused by the uneven Na deposition.[18,53,57] In contrast, the 3D-printed rGO, 30%, 50% and 70% $Ti_3C_2T_x$/rGO electrodes exhibited more stable and higher CEs and longer lifespans. For example, the 3D-printed rGO, 30% and 70% $Ti_3C_2T_x$/rGO electrodes have a lifespan of 500, 800, and 600 cycles, respectively (Fig. 3e and Fig. S10†) with corresponding CE of 99.89%, 99.90%, and 99.82%, respectively (Fig. 3d and Fig. S11†). The 3D-printed 50% $Ti_3C_2T_x$/rGO electrode exhibits the most stable cycling performance and the highest CE of 98.78% for the first cycle and eventually maintains a stable CE of 99.91% after 1800 cycles (Fig. 3d). It is worth noting that even at an ultra-large areal

capacity of 50 mA h cm^{-2} at 5 mA cm^{-2}, the 3D-printed 50% $Ti_3C_2T_x$/rGO electrode can still cycle for more than 1400 h (Fig. 3f).

The electrochemical performance was also evaluated through the symmetric cell. Prior to the measurement, the Na@$Ti_3C_2T_x$/rGO anode was fabricated by pre-deposition of 8 mA h cm^{-2} Na into the $Ti_3C_2T_x$/rGO electrode by the electrochemical deposition method. Then, the performance of the symmetric cells was measured based on the symmetric Na@$Ti_3C_2T_x$/rGO electrodes at a current density of 2 mA cm^{-2} with 2 mA h cm^{-2} as shown in Fig. 3g. It is clear to see that the Na@50% $Ti_3C_2T_x$/rGO symmetric cell can stably cycle for 1200 h with smooth and stable voltage profiles, while the Na@30% $Ti_3C_2T_x$/rGO and Na@70% $Ti_3C_2T_x$/rGO symmetric cells can operate for 990 and 930 h, respectively. In comparison, the Na@rGO symmetric cell exhibits unstable and fluctuate voltage profiles, even short-circuited after 470 h of operation. The above results indicate that the 50% $Ti_3C_2T_x$/rGO electrode exhibits the best electrochemical performance with the highest CE and the longest life span.

To further verify the fast reaction kinetics of the 3D-printed $Ti_3C_2T_x$/rGO electrode, the exchange current density was measured from the Tafel plots as shown in Fig. 3h. It is clear that the 3D-printed 50% $Ti_3C_2T_x$/rGO electrode has the highest current density of 5.01 mA cm^{-2}, which is much higher than 0.16 mA cm^{-2} (3D printed rGO electrode) and 0.02 mA cm^{-2} (2D planar Cu electrode) (Fig. 3h and Table S1†). Since a high exchange current density means a fast electrochemical reaction occurred and a lower diffusion barrier at the interface, Na metal can be uniformly deposited with fast charge transfer at the surface of the current collector.[58–60] In other words, higher exchange current densities indicate the faster transfer of sodium ions from the electrolyte to the electrode interface and
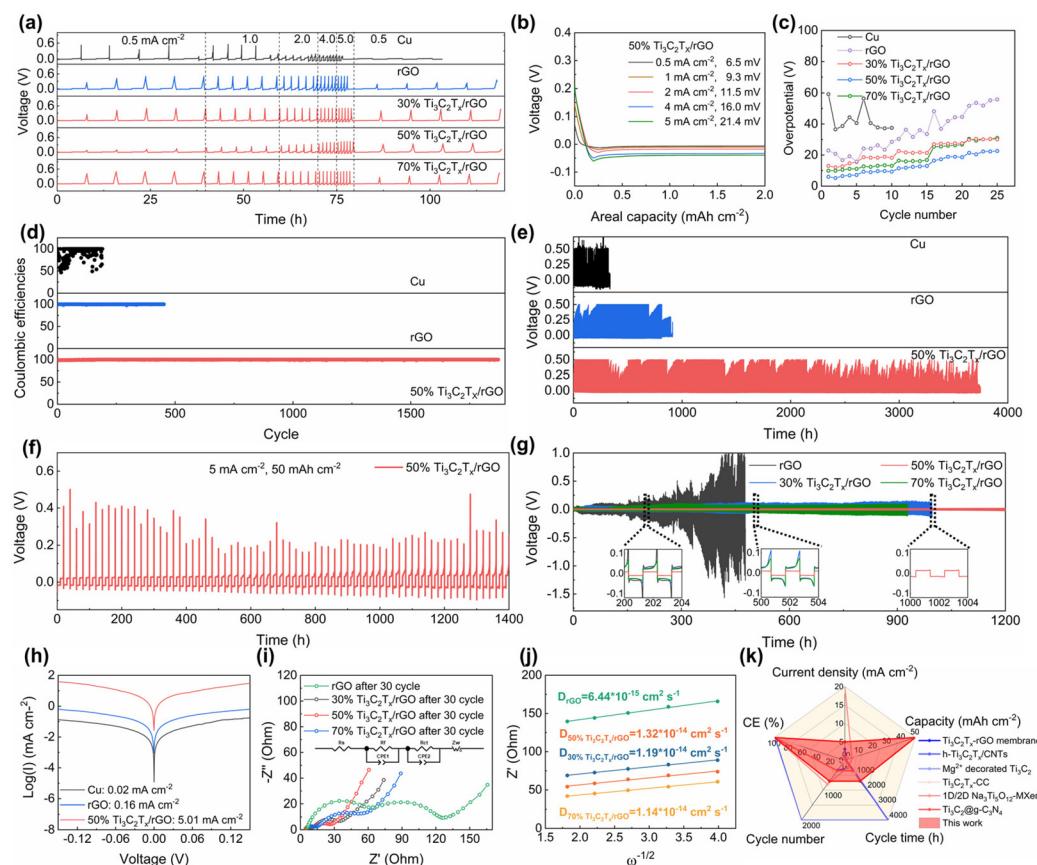
Fig. 3 Electrochemical performance of Na metal deposition/stripping on 2D planar Cu foil, 3D-printed rGO and Ti$_3$C$_2$T$_x$/rGO electrodes. (a) Rate performance of various electrodes at current densities ranging from 0.5 to 5 mA cm^{-2} with a fixed capacity of 2 mA h cm^{-2}. (b) Voltage−capacity curves the 50% Ti$_3$C$_2$T$_x$/rGO electrode at different current densities. (c) Nucleation overpotentials of Cu, 3D-printed rGO, 30%, 50% and 70% Ti$_3$C$_2$T$_x$/rGO electrodes at different current densities. (d) CEs and (e) long cycle performances of Cu, 3D-printed rGO, and 50% Ti$_3$C$_2$T$_x$/rGO electrodes at 2 mA cm^{-2} with 2 mA h cm^{-2}. (f) Long cycle performance of the 3D-printed 50% Ti$_3$C$_2$T$_x$/rGO electrode at 5.0 mA cm^{-2} with 50 mA h cm^{-2}. (g) Long cycle stability of the symmetrical cells with the 3D-printed rGO, 30%, 50% and 70% Ti$_3$C$_2$T$_x$/rGO electrodes at 2 mA cm^{-2} with 2 mA h cm^{-2}. Insets show the enlarged voltage profiles at 200, 500 and 1000 h. (h) Tafel curves of Cu, 3D-printed rGO and 50% Ti$_3$C$_2$T$_x$/rGO electrodes after 30 cycles. (i) EIS curves of 3D-printed rGO, 30%, 50%, 70% Ti$_3$C$_2$T$_x$/rGO aerogel electrodes after 30 cycles at 2 mA cm^{-2} with 2 mA h cm^{-2}. The inset in (i) shows the equivalent circuit used for EIS fitting. (j) Diffusion coefficients of 3D-printed rGO, 30%, 50%, and 70% Ti$_3$C$_2$T$_x$/rGO electrodes calculated after 30 cycles. (k) Radar charts of the electrochemical performance comparison of various Ti$_3$C$_2$T$_x$ MXene-based Na metal anodes.

the enhanced sodium plating/stripping kinetics. To gain deeper insights into the surface dynamics, the charge transfer resistance (R_{ct}) and diffusion coefficient (D) were calculated based on electrochemical impedance spectroscopy (EIS) curves. The results are shown in Fig. 3i, j, Fig. S12 and Table S2.† The R_{ct} of the 3D-printed rGO electrode before cycling is 546.89 Ω, while the R_{ct} of the 3D-printed 30%, 50% and 70% Ti$_3$C$_2$T$_x$/rGO electrodes are 353.57, 112.17 and 299.15 Ω, respectively (Fig. S12†). The R_{ct} of the 3D-printed rGO electrode decreased to 62.53 Ω after 30 cycles, while the R_{ct} of 3D-printed 30%, 50% and 70% Ti$_3$C$_2$T$_x$/rGO electrodes decreased to 25.49, 16.21 and 40.23 Ω, respectively (Fig. 3i). However, the R_{ct} increased when the Ti$_3$C$_2$T$_x$ ratio was higher than 50%. The possible reason for this is the limited surface area of the 3D-printed 70% Ti$_3$C$_2$T$_x$/rGO electrodes and the reduced pore size, which leads to a slower charge transfer rate and a higher R_{ct}. This phenomenon is agreed well with previous

reports.[18,41,61] Moreover, the diffusion coefficient of the 3D-printed 50% Ti$_3$C$_2$T$_x$/rGO electrode is 1.32 × 10^{-14} cm^2 s^{-1}, which is the highest among these electrodes (Fig. 3j and Table S2†). The above results indicate that the 3D-printed 50% Ti$_3$C$_2$T$_x$/rGO electrodes have small charge transfer resistance during cycling.[62] According to the nucleation barrier equation proposed by Barton et al.:[63]

$$\eta = \frac{i}{i_0}\frac{RT}{F} + \frac{irRT}{DcF^2} + \frac{2\gamma_{NE}V_m}{Fr}$$

where η, i, i_0, D, c, R, r, F, T, V_m and γ_{NE} are the total overpotential associated with the Na nucleation, current density, exchange current density, Na$^+$ diffusion coefficient, Na$^+$ diffusion concentration, universal gas constant, radius of the nucleation tip, Faraday constant, temperature, molar volume of Na and nuclei/electrolyte interfacial energy, respectively. From this equation, it is clear to see that the overpotential can

be affected by many factors. One of the main factors is related to the diffusion coefficient D which is inversely proportional to the overpotential.[64] The diffusion coefficient is related to the R_{ct}. The smaller R_{ct} of the 3D-printed 50% $Ti_3C_2T_x$/rGO electrode suggests that a faster charge transfer and ion diffusion ability at the electrode, resulting in a lower nucleation overpotential. This is also validated by the lower nucleation overpotential measured for the 3D-printed 50% $Ti_3C_2T_x$/rGO electrode as described previously. Since the 3D-printed 50% $Ti_3C_2T_x$/rGO electrode exhibits the best performance among the 3D-printed MXene/rGO electrodes, further characterization and mechanism investigations are based on the 50% $Ti_3C_2T_x$/rGO electrode. Furthermore, we compared our results with previous work on $Ti_3C_2T_x$ for sodium metal anodes (Fig. 3k and Table S3†).[27,33,35,37–39,65] The results show that the 3D-printed 50% $Ti_3C_2T_x$/rGO electrodes have significant advantages in terms of areal capacity, CE and long term of lifespan.

To explore the excellent electrochemical performance of the 3D-printed $Ti_3C_2T_x$/rGO electrodes, the current distribution over the surface of the electrodes and the morphological evolution of the electrodes during sodium deposition were explored by finite simulation, *ex situ* SEM and *in situ* optical microscopy characterization, respectively. As shown in Fig. 4a–c, COMSOL Multiphysics was employed to simulate the local current distribution on the electrode surface. The results show that the intrinsic protruding tip on the Cu electrode with a limited surface area results in the accumulation of higher current density in localized regions. For the 3D-printed rGO electrode, the local current density is much lower than that of the Cu electrode due to the large surface area provided by the 3D-printed rGO structure.[47] However, it is still difficult to avoid the high current distributed at the top surface of the 3D-printed rGO microlattice aerogel due to the sodiophobic properties of rGO and the tip effect.[66,67] Thus, this "tip effect" led to the accumulation and enlargement of Na ions at the tips
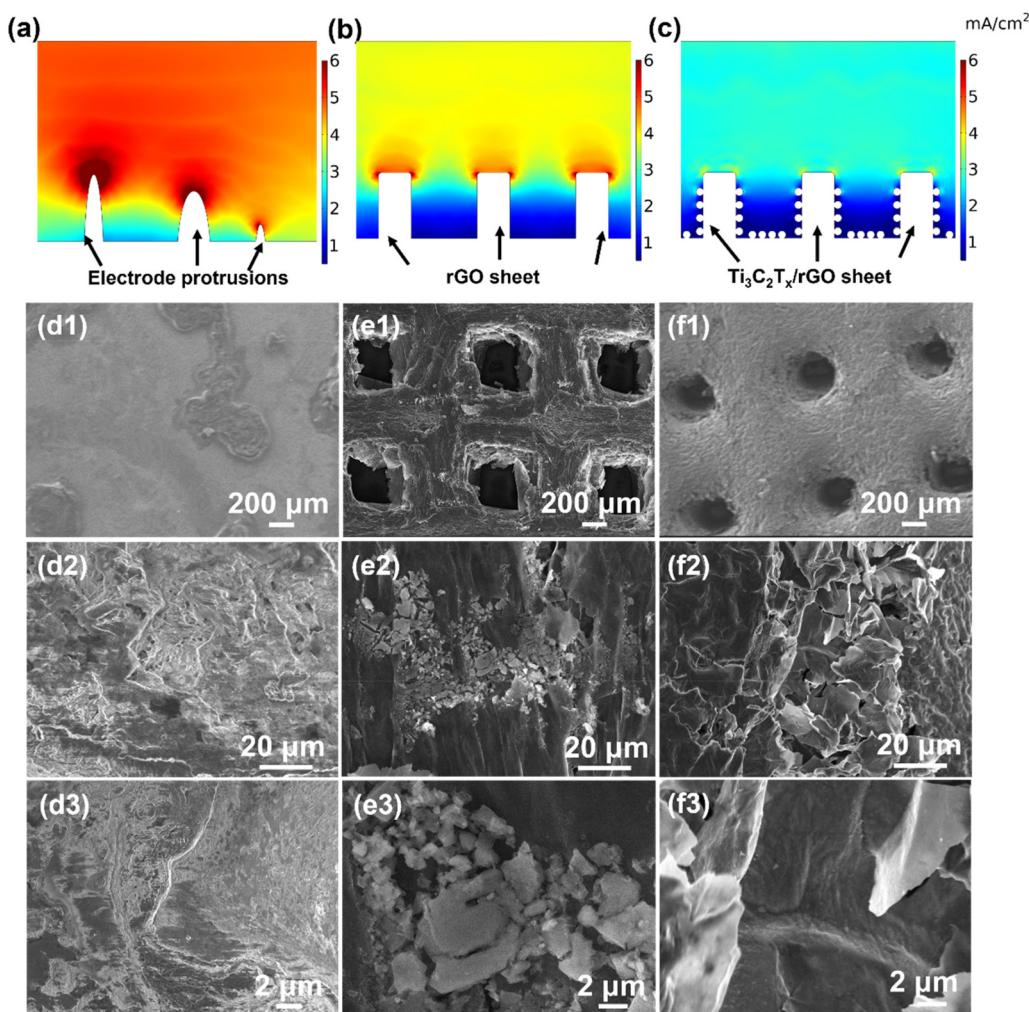
Fig. 4 Surface current density distribution simulated by COMSOL Multiphysics on (a) Cu, (b) 3D-printed rGO and (c) 3D-printed 50% $Ti_3C_2T_x$/rGO electrodes. SEM images of (d) Cu, (e) 3D-printed rGO and (f) 3D-printed 50% $Ti_3C_2T_x$/rGO electrodes after 100 cycles at 2 mA cm^{-2} with 2 mA h cm^{-2}.

over time and caused the dendrite formation during the deposition process.[66,68] In contrast, the nucleation and deposition of Na ions are more uniform due to the large surface area of the 3D-printed skeleton and the sodiophilic nature of the $Ti_3C_2T_x$ nanosheets due to the –F, –O functional groups on the surface (Fig. 4c). Thus, $Ti_3C_2T_x$ nanosheets can effectively guide the Na homogeneous nucleation and deposition.[69,70] Furthermore, to verify the reason for the excellent performance of the 3D-printed electrode, the morphology evolution of the electrodes after 100 cycles at 2 mA cm^{-2} with 2 mA h cm^{-2} was investigated using the *ex situ* SEM technique. It is obvious that there is no dead Na on the surface of the 3D-printed 50% $Ti_3C_2T_x$/rGO electrode after 100 cycles with a clear SEI film on the surface (Fig. 4f3). In contrast a large amount of dead Na dendrites are observed on the surface of Cu, with a split SEI

film (Fig. 4d3). Similarly, dead Na residues are also observed on the surface of rGO (Fig. 4e3).

More specific morphological evolution of the electrodes during sodium deposition/stripping was further systematically investigated using the *ex situ* SEM technique as shown in Fig. 5a and Fig. S13–S15.† For the Cu, 3D-printed rGO, and 50% $Ti_3C_2T_x$/rGO electrodes, sodium metal was deposited at 0.2 mA cm^{-2} with deposition amounts of 0.2, 1, and 2 mA h cm^{-2}, and then the stripping capacities were set as 0.2, 1, and 2 mA h cm^{-2} at 0.2 mA cm^{-2}. For the 3D-printed 50% $Ti_3C_2T_x$/rGO electrode, it can be observed that with deposited sodium increases, sodium is uniformly deposited over the $Ti_3C_2T_x$/rGO skeleton. After stripping with 2 mA h cm^{-2}, there is no residue of dead Na found on the surface (Fig. 5a). The corresponding deposition–stripping curve is shown in Fig. S13.† In contrast,
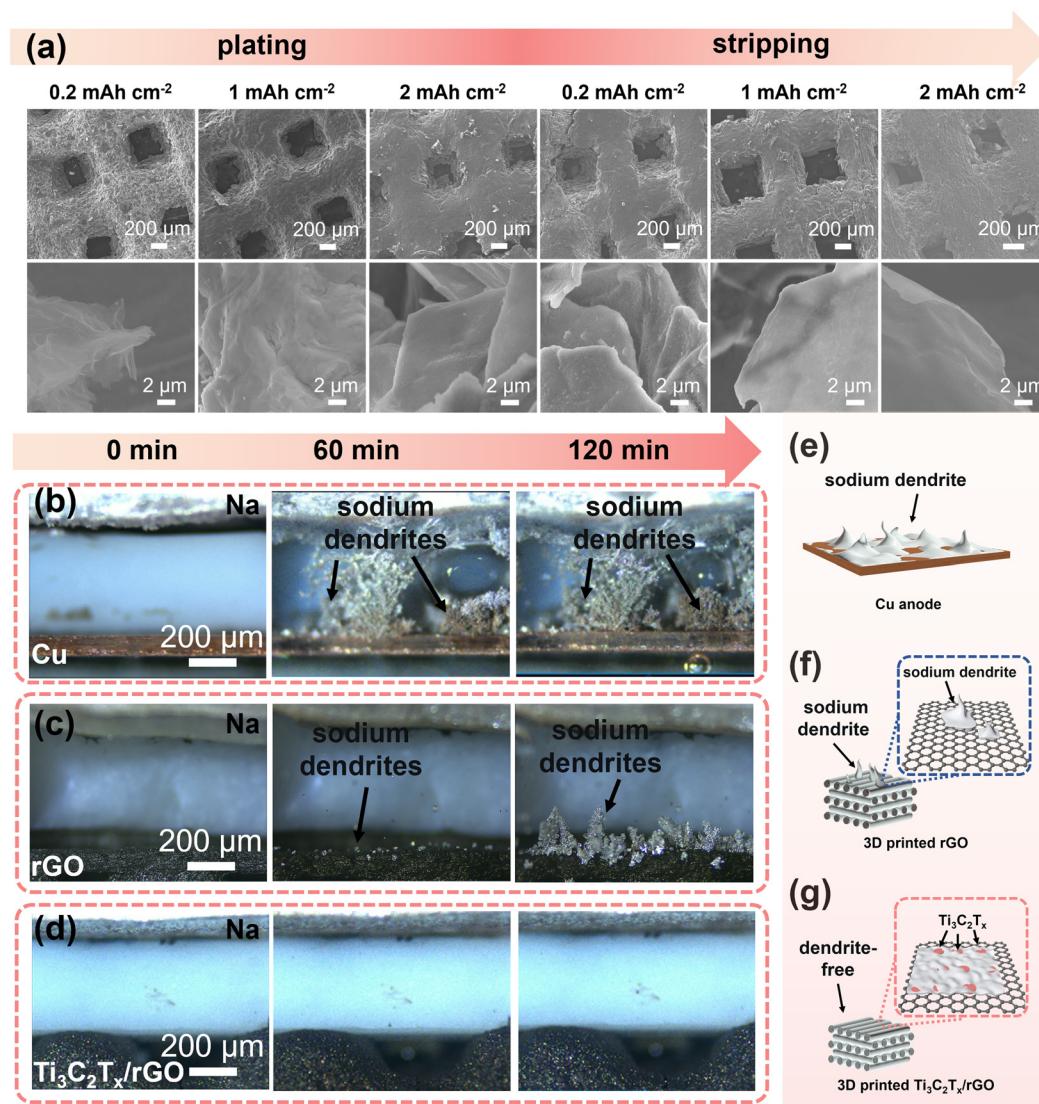

Fig. 5 (a) Morphology evolution of sodium deposition/stripping on the 3D-printed 50% $Ti_3C_2T_x$/rGO electrode with deposition capacities of 0.2, 1, and 2 mA h cm^{-2}, and stripping capacities of 0.2, 1, and 2 mA h cm^{-2} (from left to right). *In situ* optical photograph of (b) Cu, (c) 3D-printed rGO and (d) 3D-printed 50% $Ti_3C_2T_x$/rGO electrodes at 5 mA cm^{-2}. Schematic diagrams of sodium deposited on (e) Cu, (f) 3D-printed rGO and (g) 3D-printed 50% $Ti_3C_2T_x$/rGO electrodes.

Na dendrites gradually appear on the Cu electrode with increasing Na deposition, and there are plenty of dead Na dendrites after stripping 2 mA h cm^{-2} (Fig. S14†).[71] For the rGO electrode, some increased Na dendrites can be seen on the surface when deposition reached 2 mA h cm^{-2}, and mossy-like Na dendrites can be observed, and some Na metals are hardly stripped after stripping with a capacity of 2 mA h cm^{-2} (Fig. S15†). These results are consistent with our previous study.[47,71]

Macroscopic observation of Na metal deposition was made by *in situ* optical microscopy at a current density of 5 mA cm^{-2}. As shown in Fig. 5b–d, after 60 min of deposition, the Cu electrode surface was full of dendrites until short-circuited (Fig. 5b and e). The 3D-printed rGO electrode surface was grown with some sodium nucleated particles. After 120 min deposition, Na dendrites grew larger and larger on the 3D-printed rGO

surface (Fig. 5c and f). In contrast, there are no obvious dendrites formed on the 3D-printed 50% Ti$_3$C$_2$T$_x$/rGO electrode even after 120 min deposition at a high current density of 5 mA cm^{-2} (Fig. 5d and g). The above results prove that the addition of Ti$_3$C$_2$T$_x$ nanosheets can effectively alleviate the generation of sodium dendrites.[72]

To further investigate the application of Ti$_3$C$_2$T$_x$/rGO, we assembled a full cell with a Na@Ti$_3$C$_2$T$_x$/rGO anode and a 3D-printed NVP@C–rGO cathode (Fig. 6). Na@Ti$_3$C$_2$T$_x$/rGO was fabricated by electrodepositing 2.0 mA h cm^{-2} of Na metal with a current density of 0.1 mA cm^{-2} into the Ti$_3$C$_2$T$_x$/rGO electrode. An optical photograph of the Na@Ti$_3$C$_2$T$_x$/rGO electrode is shown in Fig. S16.† The 3D-printed NVP@C–rGO cathode can deliver discharge and charge capacities of 95.89 and 92.72 mA h g^{-1}, respectively (Fig. 6b). Fig. 6c shows the rate capability of the 3D-printed Na@Ti$_3$C$_2$T$_x$/rGO∥NVP@C–
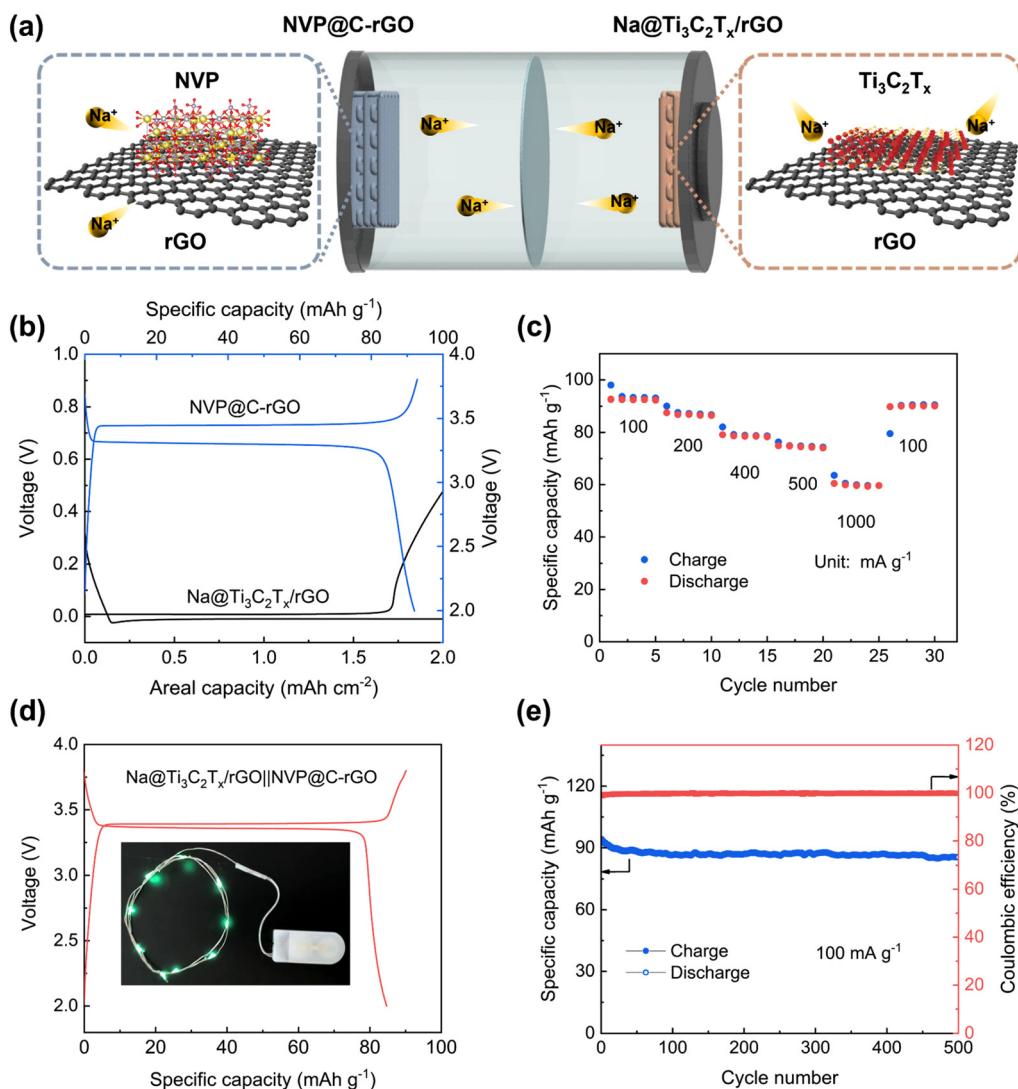
Fig. 6 Electrochemical performance evaluation of a Na@Ti$_3$C$_2$T$_x$/rGO∥NVP@C–rGO full battery. (a) A schematic diagram. (b) GCD curves of the NVP@C–rGO cathode and Na@Ti$_3$C$_2$T$_x$/rGO anode. (c) Rate performance evaluated at the current density ranging from 100 to 1000 mA g^{-1}. (d) GCD curve of the full battery at 100 mA g^{-1} at the 1st cycle. The inset shows two assembled coin cells connected in series to power light strips. (e) Cycling performance and the related CE at 100 mA g^{-1}.

rGO full battery. At current densities of 100, 200, 400, 500 and 1000 mA g^{-1}, the cell can maintain reversible discharge capacities of 92.63, 87.55, 79.11, 74.91 and 60.5 mA h g^{-1}, respectively. The charge and discharge capacities of the full cell at the first cycle are 94.87 and 89.16 mA h g^{-1}, respectively, with a high initial CE of 93.98% (Fig. 6d). Remarkably, the Na@Ti$_3$C$_2$T$_x$/rGO‖NVP@C–rGO full cell can deliver a high specific capacity of 85.3 mA h g^{-1} after 500 cycles, with an average CE of 99.80% at 100 mA g^{-1} (Fig. 6e).

4. Conclusion

In summary, 3D-printed 50% Ti$_3$C$_2$T$_x$/rGO microlattice aerogels were fabricated and further adopted as the skeleton of Na metal anodes. The obtained Ti$_3$C$_2$T$_x$/rGO skeleton electrode exhibits excellent sodiophilicity, which can promote the rapid diffusion of Na$^+$ ions and lower the nucleation barrier for Na uniform deposition. The electrochemical results show that the 3D-printed Ti$_3$C$_2$T$_x$/rGO electrode exhibits excellent electrochemical reversibility, stability and cycle life. The 3D-printed 50% Ti$_3$C$_2$T$_x$/rGO electrode achieves a long cycle life of 3600 h at 2 mA cm^{-2} with 2 mA h cm^{-2}. Impressively, it can even operate for more than 1400 h at an ultra-high areal capacity of 50 mA h cm^{-2} at a high current density of 5.0 mA cm^{-2}. The excellent electrochemical performance of the 3D-printed Ti$_3$C$_2$T$_x$/rGO electrode can be attributed to the dendrite-free deposition behavior due to the sodiophilic Ti$_3$C$_2$T$_x$ MXene and special dedicated 3D-printed artificial structure induced uniform morphology as investigated by infinite simulation and *ex situ* SEM and *in situ* optical microscopy characterization. Furthermore, a 3D-printed full cell assembled with a Na@Ti$_3$C$_2$T$_x$/rGO anode and a 3D-printed NVP@C–rGO cathode was demonstrated. The full cell can deliver a high specific capacity of 85.3 mA h g^{-1} even after 500 cycles. This well-designed 3D-printed Ti$_3$C$_2$T$_x$/rGO anode provides valuable insights for the development of high performance Na metal anodes.

Conflicts of interest

The authors declare no conflict of interest.

Acknowledgements

References

1 C. Zhao, Q. Wang, Z. Yao, J. Wang, B. Sánchez-Lengeling, F. Ding, X. Qi, Y. Lu, X. Bai, B. Li, H. Li, A. Aspuru-Guzik, X. Huang, C. Delmas, M. Wagemaker, L. Chen and Y.-S. Hu, *Science*, 2020, **370**, 708–711.

2 Y. Li, Q. Zhou, S. Weng, F. Ding, X. Qi, J. Lu, Y. Li, X. Zhang, X. Rong, Y. Lu, X. Wang, R. Xiao, H. Li, X. Huang, L. Chen and Y.-S. Hu, *Nat. Energy*, 2022, **7**, 511–519.

3 B. Lee, E. Paek, D. Mitlin and S. W. Lee, *Chem. Rev.*, 2019, **119**, 5416–5460.

4 R. Xu, Y. Xiao, R. Zhang, X. B. Cheng, C. Z. Zhao, X. Q. Zhang, C. Yan, Q. Zhang and J. Q. Huang, *Adv. Mater.*, 2019, **31**, 1808392.

5 Z. Xu, Z. Guo, R. Madhu, F. Xie, R. Chen, J. Wang, M. Tebyetekerwa, Y.-S. Hu and M.-M. Titirici, *Energy Environ. Sci.*, 2021, **14**, 6381–6393.

6 Y. Wang, Y. V. Lim, S. Huang, M. Ding, D. Kong, Y. Pei, T. Xu, Y. Shi, X. Li and H. Y. Yang, *Nanoscale*, 2020, **12**, 4341–4351.

7 W. Liu, P. Liu and D. Mitlin, *Chem. Soc. Rev.*, 2020, **49**, 7284–7300.

8 B. Sun, P. Xiong, U. Maitra, D. Langsdorf, K. Yan, C. Wang, J. Janek, D. Schroder and G. Wang, *Adv. Mater.*, 2020, **32**, 1903891.

9 X. Li, C. Zhuang, J. Xu, L. Li, T. Xu, S. Dai, X. Wang, X. Li and Y. Wang, *Nanoscale*, 2021, **13**, 8199–8209.

10 X. Zheng, Z. Gu, X. Liu, Z. Wang, J. Wen, X. Wu, W. Luo and Y. Huang, *Energy Environ. Sci.*, 2020, **13**, 1788–1798.

11 M. Zhu, G. Wang, X. Liu, B. Guo, G. Xu, Z. Huang, M. Wu, H. K. Liu, S. X. Dou and C. Wu, *Angew. Chem., Int. Ed.*, 2020, **59**, 6596–6600.

12 B. Tian, Z. Huang, X. Xu, X. Cao, H. Wang, T. Xu, D. Kong, Z. Zhang, J. Xu, J. Zang, X. Li and Y. Wang, *J. Mater. Sci. Technol.*, 2023, **132**, 50–58.

13 B. Sun, P. Li, J. Zhang, D. Wang, P. Munroe, C. Wang, P. H. L. Notten and G. Wang, *Adv. Mater.*, 2018, **30**, 1801334.

14 D. Wang, Y. Liu, G. Li, C. Qin, L. Huang and Y. Wu, *Adv. Funct. Mater.*, 2021, **31**, 2106740.

15 B. D. L. Campeon, C. Wang and Y. Nishina, *Nanoscale*, 2020, **12**, 21780–21787.

16 X. Li, J. Fu, Y. Sun, M. Sun, S. Cheng, K. Chen, X. Yang, Q. Lou, T. Xu, Y. Shang, J. Xu, Q. Chen and C. Shan, *Nanoscale*, 2019, **11**, 13343–13353.

17 Y. Zhuang, D. Deng, L. Lin, B. Liu, S. Qu, S. Li, Y. Zhang, B. Sa, L. Wang, Q. Wei, L. Mai, D.-L. Peng and Q. Xie, *Nano Energy*, 2022, **97**, 107202.

18 Z. Wang, Z. Huang, H. Wang, W. Li, B. Wang, J. Xu, T. Xu, J. Zang, D. Kong, X. Li, H. Y. Yang and Y. Wang, *ACS Nano*, 2022, **16**, 9105–9116.

19 H. Jiang, Q. Dong, M. Bai, F. Qin, M. Yi, J. Lai, B. Hong and Y. Lai, *Nanoscale*, 2021, **13**, 3144–3152.

20 P. Liu, H. Yi, S. Zheng, Z. Li, K. Zhu, Z. Sun, T. Jin and L. Jiao, *Adv. Energy Mater.*, 2021, **11**, 2101976.

21 X. Zhang, P. He, B. Dong, N. Mu, Y. Liu, T. Yang and R. Mi, *Nanoscale*, 2021, **13**, 4167–4176.

22 J. Xu, H. Tang, T. Xu, D. Wu, Z. Shi, Y. Tian and X. Li, *Ionics*, 2017, **23**, 3273–3280.

23 C. Qin, D. Wang, Y. Liu, P. Yang, T. Xie, L. Huang, H. Zou, G. Li and Y. Wu, *Nat. Commun.*, 2021, **12**, 7184.

24 B. Ke, X. Wang, S. Cheng, W. Li, R. Deng, C. Zhang, J. Lin, Q. Xie and D.-L. Peng, *Sci. China Mater.*, 2023, **66**, 118–126.

25 X. Li, Z. Huang, C. E. Shuck, G. Liang, Y. Gogotsi and C. Zhi, *Nat. Rev. Chem.*, 2022, **6**, 389–404.

26 N. Li, Y. Zhan, H. Wu, J. Fan and J. Jia, *Nanoscale*, 2022, **14**, 17027–17035.

27 Y. Fang, Y. Zhang, K. Zhu, R. Lian, Y. Gao, J. Yin, K. Ye, K. Cheng, J. Yan, G. Wang, Y. Wei and D. Cao, *ACS Nano*, 2019, **13**, 14319–14328.

28 M. Lu, W. Han, H. Li, W. Shi, J. Wang, B. Zhang, Y. Zhou, H. Li, W. Zhang and W. Zheng, *Energy Storage Mater.*, 2019, **16**, 163–168.

29 M. Lu, H. Li, W. Han, J. Chen, W. Shi, J. Wang, X.-M. Meng, J. Qi, H. Li, B. Zhang, W. Zhang and W. Zheng, *J. Energy Chem.*, 2019, **31**, 148–153.

30 D. Yan, H. Y. Yang and Y. Bai, *Nano Res.*, 2023, **16**, 8173–8190.

31 C. J. Zhang, L. McKeon, M. P. Kremer, S. H. Park, O. Ronan, A. Seral-Ascaso, S. Barwich, C. O. Coileain, N. McEvoy, H. C. Nerl, B. Anasori, J. N. Coleman, Y. Gogotsi and V. Nicolosi, *Nat. Commun.*, 2019, **10**, 1795.

32 D. Er, J. Li, M. Naguib, Y. Gogotsi and V. B. Shenoy, *ACS Appl. Mater. Interfaces*, 2014, **6**, 11173–11179.

33 C. Bao, J. Wang, B. Wang, J. Sun, L. He, Z. Pan, Y. Jiang, D. Wang, X. Liu, S. X. Dou and J. Wang, *ACS Nano*, 2022, **16**, 17197–17209.

34 Z. Yang, Y. Zheng, W. Li and J. Zhang, *Nanoscale*, 2021, **13**, 11534–11543.

35 X. He, S. Jin, L. Miao, Y. Cai, Y. Hou, H. Li, K. Zhang, Z. Yan and J. Chen, *Angew. Chem., Int. Ed.*, 2020, **59**, 16705–16711.

36 K. Lee, Y. J. Lee, M. J. Lee, J. Han, J. Lim, K. Ryu, H. Yoon, B. H. Kim, B. J. Kim and S. W. Lee, *Adv. Mater.*, 2022, **34**, 2109767.

37 H. Jiang, X. Lin, C. Wei, Y. Zhang, J. Feng and X. Tian, *Small*, 2022, **18**, 2107637.

38 Y. Fang, R. Lian, H. Li, Y. Zhang, Z. Gong, K. Zhu, K. Ye, J. Yan, G. Wang, Y. Gao, Y. Wei and D. Cao, *ACS Nano*, 2020, **14**, 8744–8753.

39 J. Luo, X. Lu, E. Matios, C. Wang, H. Wang, Y. Zhang, X. Hu and W. Li, *Nano Lett.*, 2020, **20**, 7700–7708.

40 J. Yan, G. Zhi, D. Kong, H. Wang, T. Xu, J. Zang, W. Shen, J. Xu, Y. Shi, S. Dai, X. Li and Y. Wang, *J. Mater. Chem. A*, 2020, **8**, 19843–19854.

41 Y. Liu, H. Wang, H. Yang, Z. Wang, Z. Huang, D. Pan, Z. Zhang, Z. Duan, T. Xu, D. Kong, X. Li, Y. Wang and J. Sun, *ACS Nano*, 2023, **17**, 10844–10856.

42 X. B. Cheng, R. Zhang, C. Z. Zhao and Q. Zhang, *Chem. Rev.*, 2017, **117**, 10403–10473.

43 H. Zhao, C. Zhuang, J. Xu, Z. Zhang, W. Shen, H. Tang, Y. Wang, T. Xu, X. Wang and X. Li, *Ionics*, 2020, **26**, 5019–5028.

44 J. Guo, H. Pei, Y. Dou, S. Zhao, G. Shao and J. Liu, *Adv. Funct. Mater.*, 2021, **31**, 2010499.

45 Y. Xie, J. Ao, L. Zhang, Y. Shao, H. Zhang, S. Cheng and X. Wang, *Chem. Eng. J.*, 2023, **451**, 139017.

46 Y. Xie, W. Zheng, J. Ao, Y. Shao, X. Huang, H. Li, S. Cheng and X. Wang, *Energy Storage Mater.*, 2023, **62**, 102925.

47 J. Yan, S. Huang, Y. V. Lim, T. Xu, D. Kong, X. Li, H. Y. Yang and Y. Wang, *Mater. Today*, 2022, **54**, 110–152.

48 K. Chen, X. Li, J. Zang, Z. Zhang, Y. Wang, Q. Lou, Y. Bai, J. Fu, C. Zhuang, Y. Zhang, L. Zhang, S. Dai and C. Shan, *Nanoscale*, 2021, **13**, 12370–12378.

49 Q. Deng, X. Liu, Z. Li, H. Fan, Y. Zhang and H. Y. Yang, *J. Colloid Interface Sci.*, 2023, **633**, 480–488.

50 J. Guo, Y. Huang, S. Zhao, Z. Li, Z. Wang, G. Shao and J. Liu, *ACS Nano*, 2021, **15**, 16322–16334.

51 M. Ghidiu, M. R. Lukatskaya, M. Q. Zhao, Y. Gogotsi and M. W. Barsoum, *Nature*, 2014, **516**, 78–81.

52 W. S. Hummers, Jr. and R. E. Offeman, *J. Am. Chem. Soc.*, 1958, **80**, 1339–1339.

53 H. Wang, W. Bai, H. Wang, D. Kong, T. Xu, Z. Zhang, J. Zang, X. Wang, S. Zhang, Y. Tian, X. Li, C.-S. Lee and Y. Wang, *Energy Storage Mater.*, 2023, **55**, 631–641.

54 B. Anasori, M. R. Lukatskaya and Y. Gogotsi, *Nat. Rev. Mater.*, 2017, **2**, 16098.

55 H. Zeng, Z. Li, G. Li, X. Cui, M. Jin, T. Xie, L. Liu, M. Jiang, X. Zhong, Y. Zhang, H. Zhang, K. Ba, Z. Yan, Y. Wang, S. Song, K. Huang and S. Feng, *Adv. Energy Mater.*, 2021, **12**, 2102765.

56 H. Shi, C. J. Zhang, P. Lu, Y. Dong, P. Wen and Z. S. Wu, *ACS Nano*, 2019, **13**, 14308–14318.

57 R. Deng, B. Ke, Y. Xie, S. Cheng, C. Zhang, H. Zhang, B. Lu and X. Wang, *Nano-Micro Lett.*, 2023, **15**, 73.

58 Z. Ju, C. Jin, H. Yuan, T. Yang, O. Sheng, T. Liu, Y. Liu, Y. Wang, F. Ma, W. Zhang, J. Nai and X. Tao, *Chem. Eng. J.*, 2021, **408**, 128016.

59 X. Xiong, W. Yan, Y. Zhu, L. Liu, L. Fu, Y. Chen, N. Yu, Y. Wu, B. Wang and R. Xiao, *Adv. Energy Mater.*, 2022, **12**, 2103112.

60 Q. Zhao, Z. Tu, S. Wei, K. Zhang, S. Choudhury, X. Liu and L. A. Archer, *Angew. Chem., Int. Ed.*, 2018, **57**, 992–996.

61 L. Hou, L. Zhang, J. Zang, W. Shen, T. Zhang, X. Huang, H. Yuan, D. Kong, Y. Wang, X. Li and T. Xu, *J. Phys. D: Appl. Phys.*, 2022, **55**, 234002.

62 T. Wang, J. Duan, B. Zhang, W. Luo, X. Ji, H. Xu, Y. Huang, L. Huang, Z. Song, J. Wen, C. Wang, Y. Huang and J. B. Goodenough, *Energy Environ. Sci.*, 2022, **15**, 1325–1333.

63 J. L. Barton and J. O'M. Bockeris, *Proc. R. Soc. London, Ser. A*, 1962, **268**, 485–505.

64 H. Wang, E. Matios, J. Luo and W. Li, *Chem. Soc. Rev.*, 2020, **49**, 3783–3805.

65 B. Wang, T. Jiang, L. Hou, H. Wang, T. Xu, Z. Zhang, D. Kong, X. Li and Y. Wang, *Solid State Ionics*, 2021, **368**, 115711.

66 C. P. Yang, Y. X. Yin, S. F. Zhang, N. W. Li and Y. G. Guo, *Nat. Commun.*, 2015, **6**, 8058.

67 Z. Huang, Z. Wang, X. Wang, S. Zhang, T. Xu, Z. Zhang, J. Zang, D. Kong, X. Li and Y. Wang, *Solid State Ionics*, 2022, **380**, 115941.

68 B. Tian, Z. Huang, H. Yang, H. Wang, T. Xu, D. Kong, C. Gao, J. Zang, X. Li and Y. Wang, *Ionics*, 2022, **28**, 4641–4651.

69 K. Li, M. Liang, H. Wang, X. Wang, Y. Huang, J. Coelho, S. Pinilla, Y. Zhang, F. Qi, V. Nicolosi and Y. Xu, *Adv. Funct. Mater.*, 2020, **30**, 2000842.

70 H. Tetik, J. Orangi, G. Yang, K. Zhao, S. B. Mujib, G. Singh, M. Beidaghi and D. Lin, *Adv. Mater.*, 2022, **34**, 2104980.

71 H. Yang, H. Wang, W. Li, B. Tian, T. Xu, D. Kong, S. Huang, K. Liu, X. Li, H. Y. Yang and Y. Wang, *J. Mater. Chem. A*, 2022, **10**, 16842–16852.

72 Q. Han, Y. Zhou, R. Du, B. Xiao, J. Cheng, M. Zhang, C. Dong, X. Sun, F. Jiang and J. Yang, *J. Mater. Chem. A*, 2021, **9**, 14013–14024.